

# Stellar halos tracing the assembly of Ultra-Faint Dwarf galaxies

Lapo Querci <sup>1,\*</sup>, Andrea Pallottini <sup>2</sup>, Lorenzo Branca <sup>2</sup>, and Stefania Salvadori <sup>1,3</sup>.

<sup>1</sup> Dipartimento di Fisica e Astronomia, Università degli Studi di Firenze, Via G. Sansone 1, 50019, Sesto Fiorentino, Italy

<sup>2</sup> Scuola Normale Superiore, Piazza dei Cavalieri 7, 56126 Pisa, Italy

<sup>3</sup> INAF - Osservatorio Astrofisico di Arcetri, Largo E.Fermi 5, 50125, Firenze, Italy

Received 3 October, 2024; accepted XX XXX, XXXX

## ABSTRACT

*Context.* Ultra-faint dwarfs (UFDs) are expected to be the relics of the earliest galaxies forming in the Universe. Observations show the presence of a stellar halo around them, which can give precious insights into the evolution of UFDs. Indeed, stellar halos can form via tidal interaction, early supernova feedback, or merging events.

*Aims.* This work investigates how merger properties impact the formation of stellar halos around UFDs, focusing on Tucana II, the most promising UFD assembled through mergers.

*Methods.* We develop N-body simulations of dry isolated mergers between two UFDs, resolving their stellar component down to  $1 M_{\odot}$ . We build a suite of simulations by varying: *i*) the merger mass ratio,  $M_1/M_2$ , *ii*) the specific kinetic energy,  $k$ , and *iii*) angular momentum,  $l$ , *iv*) the dark-to-stellar mass ratio,  $M_{\text{DM}}/M_{\star}$ , of the progenitors and *v*) their stellar size,  $R_{1/2}$ . To fully explore such a 5-dimensional parameter space, we train a neural network to emulate the properties of the resulting “post-merger” UFD, by quantifying the half-mass radius ( $R_{\star}$ ) and the fraction of stars at radii  $> 5R_{\star}$  ( $f_5$ ).

*Results.* Our principal component analysis clearly shows that  $f_5$  ( $R_{\star}$ ) is primarily determined by  $M_1/M_2$  ( $R_{1/2}$ ), with  $R_{1/2}$  ( $M_1/M_2$ ) playing a secondary role. Both  $f_5$  and  $R_{\star}$  show almost no dependence on  $k$ ,  $l$ , and  $M_{\text{DM}}/M_{\star}$  in the explored range. Using our emulator, we find that to form the stellar halo observed in Tucana II, i.e.  $f_5 = 10 \pm 5\%$  and  $R_{\star} = 120 \pm 30$  pc, we need to merge progenitors with  $M_1/M_2 = 8^{+4}_{-3}$ , the size of more massive one being  $R_{1/2} = 97^{+25}_{-18}$  pc. Such findings are corroborated by the consistency ( $\chi^2 \approx 0.5 - 2$ ) between stellar density profiles observed for Tucana II and those of simulations having  $M_1/M_2$  and  $R_{1/2}$  close to the values predicted by the emulator.

*Conclusions.* The stellar halos of UFDs uncover crucial information about the properties of their smaller progenitor galaxies. Ongoing and planned spectroscopic surveys will greatly increase the statistics of observed stars in UFDs and thus of their associated stellar halos. By interpreting such observations with our simulations, we will provide new insights into the assembly history of UFDs and thus on the early galaxy formation process.

**Key words.** galaxies: dwarf, evolution, interactions, Local Group – methods: numerical

## 1. Introduction

Dwarf galaxies have been extensively observed in the Local Group, where more than 70 objects have been detected as satellites orbiting around the Milky Way (MW) and Andromeda (McConnachie 2012). Among these satellites, the Ultra-Faint Dwarf galaxies (UFDs;  $M \lesssim 10^5 M_{\odot}$ , Simon 2019) are dominated by ancient,  $> 10$  Gyr (Brown et al. 2012; Gallart et al. 2021), and very metal-poor stars (Kirby et al. 2008; Spite et al. 2018) and, similarly to the classical dwarf spheroidal galaxies, have little to no gas mass (e.g., Westmeier et al. 2015). The observed properties of UFDs, which include the metallicity distribution function and the fraction of carbon-enhanced metal-poor stars (CEMP-no, e.g., Lai et al. 2011; Yoon et al. 2019) strongly support the idea that UFDs are the living relics of the first star-forming minihalos (e.g., Ricotti & Gnedin 2005; Salvadori & Ferrara 2009; Jeon et al. 2017; Rossi et al. 2024), which form before the end of Reionization and are hosted by  $10^6 - 10^7 M_{\odot}$  dark matter halos. Their early formation and low mass make them the best candidates to host first stars’ descendants (e.g., Salvadori et al. 2015; Magg et al. 2018; Rossi et al. 2024) and the perfect laboratories to study the effects of feedback processes on galaxy formation (e.g., Jeon et al. 2015; Agertz et al. 2020; Gutcke et al. 2022).

Moreover, UFDs are the most dark matter-dominated stellar system known, with mass-to-luminosity ratios  $M/L > 100 M_{\odot}/L_{\odot}$ , and their study is expected to play a key role in understanding the nature of dark matter (e.g., Bullock & Boylan-Kolchin 2017; Strigari 2018; Battaglia & Nipoti 2022).

Identifying UFD stars becomes increasingly difficult as the distance from the galactic center increases due to their faint nature and the foreground contamination of MW stars. Nonetheless, recent observations of UFDs started to provide evidence of stars at large distances from the center. This is the case of Tucana II, where stars have been identified up to  $\sim 9$  half-light radius,  $R_{1/2}$  (Chiti et al. 2021), Hercules I, with stars detected up to  $\sim 9.5 R_{1/2}$  (Garling et al. 2018; Longeard et al. 2023; Ou et al. 2024), Tucana V, up to  $\sim 10 R_{1/2}$  (Hansen et al. 2024), Ursa Major I up to  $\sim 4 R_{1/2}$ , Boötes I up to  $\sim 4 R_{1/2}$ , and Coma Berenice up to  $\sim 2 R_{1/2}$  (Waller et al. 2023). In addition, multiple studies identify new and distant stars exploiting Gaia data. Tau et al. (2024) explore the outskirts of 30 UFDs using already known and new RR Lyrae stars and show that at least  $\sim 30\%$  present extended stellar populations. By considering  $\sim 60$  MW dwarf galaxies satellites, Jensen et al. (2024) systematically identify candidate member stars based on spatial, color-magnitude, and proper motion information; they report an extended secondary outer profile for nine dwarf MW satellites, seven of which are

\* lapo.querici@unifi.it

UFDs: Boötes I, Boötes III, Draco II, Grus II, Segue I, Tucana II, Tucana III.

The formation channels for such extended features can be i) tidal stripping, ii) in situ formation via supernova (SN) feedback, iii) and merging events. Due to the proximity with the MW, its gravitational pull can deform the UFDs morphology forming an extended halo, as shown by Fattahi et al. (2018). Signatures of tidal interaction are signaled by the presence of velocity gradients (Li et al. 2018) and deviations from the expected exponential profile that typically describes the stellar density distribution (Peñarrubia et al. 2008). Early supernova feedback can induce an inside-out stellar formation, with the successive generation of stars forming at larger radii. This scenario is plausible since UFDs may have a bursty star formation history (Wheeler et al. 2019), as expected for galaxies forming most of their stars prior to the Reionization (Gelli et al. 2020, 2023; Pallottini & Ferrara 2023; Sun et al. 2023). Signs of SNe can be retrieved in the chemical composition of stars and thus high-resolution spectroscopy is the primary way to determine if the UFD stellar halos have an *in situ* origin (e.g., Chiti et al. 2023). Merger events between UFDs are expected (Deason et al. 2014; Revaz 2023) and they can form extended stellar components beyond  $5 - 20 R_{1/2}$  (Deason et al. 2022; Ricotti et al. 2022). Determining if a stellar halo formed via merging events requires a combination of spatial and chemical information to rule out the other scenarios. Currently, only in Tucana II the stellar halo seems consistent at a high confidence level with the merger scenario (Chiti et al. 2021, 2023).

Tucana II is a UFD with stellar mass  $M_{\star}^{\text{TucII}} = 3_{-2}^{+7} \times 10^3 M_{\odot}$ , half-light radius  $R_{1/2}^{\text{TucII}} = 120 \pm 30$  pc (Bechtol et al. 2015), and it has one of the lowest average metallicity in the Local Group, i.e.,  $[Fe/H] = -2.7$  (Ji et al. 2016; Chiti et al. 2018). When observing the outskirts of Tucana II, Chiti et al. (2021) identified five and two giant stars located at distances  $> 2 R_{1/2}$  and  $> 5 R_{1/2}$ , respectively. Chiti et al. (2021, 2023) ruled out the tidal interaction scenario for Tucana II because of: i) the orthogonality of the stellar extension with respect to the predicted direction of the tidal debris; ii) the absence of a velocity gradient in the extended stellar component; iii) the position of the pericenter (around  $\sim 40$  kpc; Battaglia & Nipoti 2022; Pace et al. 2022), which is distant enough to corroborate a scenario of low impact from tidal interactions. The SN feedback scenario for the formation of the stellar halo in Tucana II is disfavored for two reasons. First, Chiti et al. (2023) report that 75% of the observed metal-poor stars ( $[Fe/H] < -2.9$ ) are Carbon-enhanced (i.e., the so-called CEMP-no,  $[C/Fe] > 0.7$ ), which suggests enrichment by low-energy primordial "faint SNe" (e.g., Salvadori et al. 2015; Jeon et al. 2017; Rossi et al. 2023). Second, the chemical abundances of stars in Tucana II at various  $[Fe/H]$  are consistent with the ones observed in other UFDs. Therefore, if SN feedback is the main formation channel of stellar halos, most UFDs should present an extended feature, which instead is not observed. Ruling out the other possibilities, the remaining formation scenario for Tucana II stellar halo is the merging between two UFDs.

A result supporting such a scenario comes from the cosmological hydrodynamical simulations by Tarumi et al. (2021). They report that a galaxy closely resembling Tucana II in terms of the fraction of distant stars, metallicity, and metallicity gradient can be formed by major merger, i.e., a merger where the mass ratio between the two galaxies is within 1:1 and 10:1. There have been other studies analyzing the impact of dwarf galaxy mergers on the formation of stellar halos. Using N-body simulations, Deason et al. (2022) find that *intermediate* merger ratios ( $\sim 5:1$ )

maximize the growth of extended stellar halos regardless of the stellar mass–halo mass relation. By preparing cosmological N-body simulations, Ricotti et al. (2022) show that the shape and mass of the stellar halos can be described as the sum of nearly exponential profiles with scale radii determined by the mass ratio of the mergers building it. Goater et al. (2024) analyzed tidally isolated UFDs in zoom-in hydrodynamical simulations, taken from the EDGE cosmological simulation suite (Agertz et al. 2020), finding that many galaxies exhibit anisotropic extended stellar halos mimicking tidal tails, but such halos are actually formed by late-time mergers. These studies primarily focus on the influence of the merger mass ratio on the stellar halo formation, with limited exploration of other potential merger or progenitor characteristics, leaving open questions such as: does the merger trajectory have any impact on the stellar halo formation? Does the dark matter total mass influence the size of the post-merger galaxy or the stellar halo formation? What properties of the merger can we infer using present-day observations?

In this work, we explore the parameter space of UFD mergers, considering five key properties: specific angular momentum, specific kinetic energy, merger mass ratio, total UFD mass, and initial radius, to model the trajectory and mass ratio of the merger and the mass and radius of the progenitors. Our goal is to investigate how these parameters influence the formation of the stellar halo in UFDs. We develop a suite of N-body simulations of isolated mergers between two possible Tucana II progenitors, to perform a wide ( $>1$  dex) parameter space exploration. Ideally, we would need a large number of simulations with *single-stellar* mass resolution, to have i) a high-frequency sampling of the parameters and ii) good precision. To achieve both features, we developed an *emulator* that can efficiently generate the properties of the post-merger galaxies, once trained with simulation data. To validate our findings, we conduct a comparative analysis of simulated stellar surface density profiles with that observed in Tucana II.

This article is structured as follows. First, we describe the simulation setup, the parameter space explored, and how we construct the emulator (Sec. 2). Then, the results of the parameter space exploration and the comparison with observations are presented (Sec. 3). Finally, we summarize and discuss our findings in (Sec. 4).

## 2. Methods

Here, we present the suite of simulations for isolated merging UFD galaxies and detail our strategy for exploring the parameter space of the possible merger configurations.

We start by reviewing the base assumptions and the schemes used to generate the initial conditions for the progenitors (Sec. 2.1). Then, we discuss the intervals adopted for the initial conditions (Sec. 2.2) and show how we can explore them with a Latin hypercube sampling of the merger parameter space (Sec. 2.3). Finally, we describe the numerical code used to follow the time evolution of the merger (Sec. 2.4) and we explain how we train an emulator by using the results from our suite (Sec. 2.5).

### 2.1. Initial conditions

Our merging simulations are set up at redshift  $z = 6$ , after the Reionization of the Universe, when most of the gas of UFDs, i.e., minihalos, is expected to be removed or heated by radiation (Barkana & Loeb 1999; Sobacchi & Mesinger 2013; Gutcke et al. 2022). For this reason, we neglect the gas component and

focus on *dry* mergers, i.e., mergers of galaxies with only dark matter and stars.

Throughout the simulation suite, we vary the main properties of the dark matter and stellar component of the two merging galaxies together with the parameters defining the kinematics of the merger. Specifically, we explore i) the dark matter mass,  $M_{\text{DM}}$ ; ii) the stellar mass,  $M_{\star}$ ; iii) scale radius of the progenitors; iv) the trajectory of the merger. A detailed discussion of the ranges adopted for these quantities is given in Sec. 2.2 (see Table 1 for a summary), while, in the following, we describe the general setup and parameterization of the initial conditions.

### 2.1.1. Dark matter profile

We assume the dark matter density profile,  $\rho_{\text{DM}}$ , to be a spherically symmetric Navarro-Frank-White (Navarro et al. 1996), i.e.,

$$\rho_{\text{DM}}(r) = \frac{3M_{\text{DM}}}{4\pi R_{\text{vir}}^3} \left( \ln(1+c) - \frac{c}{1+c} \right)^{-1} \times \frac{r}{R_{\text{vir}}} \left( \frac{1}{c} + \frac{r}{R_{\text{vir}}} \right)^{-2}, \quad (1)$$

where  $r$  is the distance from the galaxy center,  $R_{\text{vir}}$  is the virial radius, and  $c$  is the concentration parameter. The definition of  $R_{\text{vir}}$  is

$$R_{\text{vir}} = \left[ \frac{(M_{\text{DM}} + M_{\star})G}{10H^2} \right]^{1/3}, \quad (2)$$

with  $G$  being the gravitational constant and  $H = H(z)$  the Hubble parameter<sup>1</sup>, i.e.,

$$H = H_0 \left[ \Omega_m(1+z)^3 + \Omega_{\Lambda} \right]^{1/2}. \quad (3)$$

The concentration is  $c = 3.5$ , assuming the results found by Diemer & Kravtsov (2015) for a galaxy of  $M_{\text{DM}} = 10^8 M_{\odot}$  at  $z = 6$ .

### 2.1.2. Stellar profile

We adopt the exponential profile, commonly utilized to fit stellar density profiles of UFDs (e.g., Belokurov et al. 2006; Martin et al. 2008; Muñoz et al. 2018). The profile is defined by

$$\rho_{\star}(r) = \rho_0 e^{-r/(0.5R_{1/2})}, \quad (4)$$

where  $\rho_0$  is the central density,  $R_{1/2}$  is the projected radius that contains half of the mass of the galaxy, i.e., the half-mass radius, and the 0.5 factor arises integrating the exponential profile, factor 0.351, and projecting the three-dimensional scale radius to the projected two-dimensional  $R_{1/2}$ , factor 1.33 (Wolf et al. 2010). In the suite, we vary  $R_{1/2}$  to account for different initial stellar densities, as discussed in Sec. 2.2.

### 2.1.3. Discretization of the progenitors

We use the public code DICE (Perret 2016) to perform a lagrangian sampling of the particles composing each progenitor in order to obtain the selected density profiles for dark matter (eq. 1) and stars (eq. 4). DICE uses an N-try Markov Chain Monte

<sup>1</sup> The cosmological parameters adopted in this work are taken from Planck Collaboration (2016):  $H_0 = 67.74 \text{ km s}^{-1} \text{ Mpc}^{-1}$ ,  $\Omega_m = 0.3089$ , and  $\Omega_{\Lambda} = 0.6911$ .

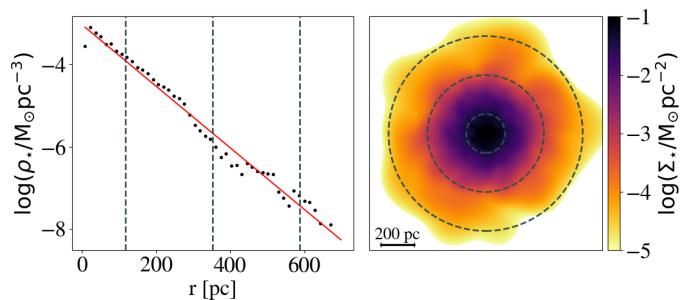


Fig. 1: Example of the virialized stellar distribution of a progenitor with  $M_{\star} = 5.48 \times 10^3 M_{\odot}$  and  $R_{1/2} = 118 \text{ pc}$  generated using DICE (see Sec. 2.1.3). **Left panel:** stellar density ( $\rho_{\star}$ ) extracted by spherically averaging the mass in a simulation shell (points) and the fitted exponential profile (solid line, eq. 4) as a function of the radius ( $r$ ). **Right panel:** stellar surface density map,  $\Sigma_{\star}$  integrated along the line of sight; the spatial scale is indicated as an inset. In both panels, the dashed lines mark the location of spheres with radius  $R_{1/2}$ ,  $3R_{1/2}$ , and  $5R_{1/2}$ .

Carlo method to extract the particles' position  $\mathbf{x}_s$  from the profiles and integrates the Jeans equations to assign the velocity  $\mathbf{v}_s$  for each particle  $s$ ; this is done separately for the progenitors.

To match the observed stellar mass of Tucana II, we fix the sum of the stellar mass of the two progenitors to  $M_{\star, \text{tot}} = 6000 M_{\odot}$ . To compare our results with star-by-star observations, we opted for a *single-stellar* mass resolution, i.e., in all the simulations the mass resolution of the stellar component is  $m_{\star} = 1 M_{\odot}$ . The number of dark matter particles is adjusted to have a mass resolution of  $m_{\text{DM}} = 100 M_{\odot}$ . The dark matter to stellar mass resolution ratio adopted is consistent with the one used in Ricotti et al. (2022) and satisfies the trade-off between computational cost and spurious numerical heating (e.g., Ludlow et al. 2023; Di Cintio 2024). The numerical heating mostly affects the size of the post-merger galaxy while is negligible for the stellar halo formation, as shown in App. A.

As an example of the procedure, in Fig. 1 we report the stellar density profile (left panel) and the stellar surface density map on the  $XY$  plane (right panel) generated by DICE for a progenitor with  $M_{\star} = 5.48 \times 10^3 M_{\odot}$  and  $R_{1/2} = 118 \text{ pc}$ . In the left panel, the solid red line shows the exponential profile fitted to the progenitor density profile. Since DICE computes galaxies at Jeans' equilibrium, the initial progenitors are not at virial equilibrium and must evolve in isolation to virialize. We address this aspect in the next paragraph (Sec. 2.1.4).

### 2.1.4. Merger setup

Using DICE, we place the two progenitors in the simulation box, assign them a relative velocity, set the system's center of mass at rest in the center, and place the progenitors at a distance  $D = 8 \text{ kpc}$  along the X-axis, which ensures that they virialize while the gravitational interaction is still negligible. Hereafter, the subscript 1 refers to the more massive progenitor and 2 to the other one.

We set the progenitors on the same Z-axis, assuming the velocity differs from zero only along the X-axis. The initial posi-

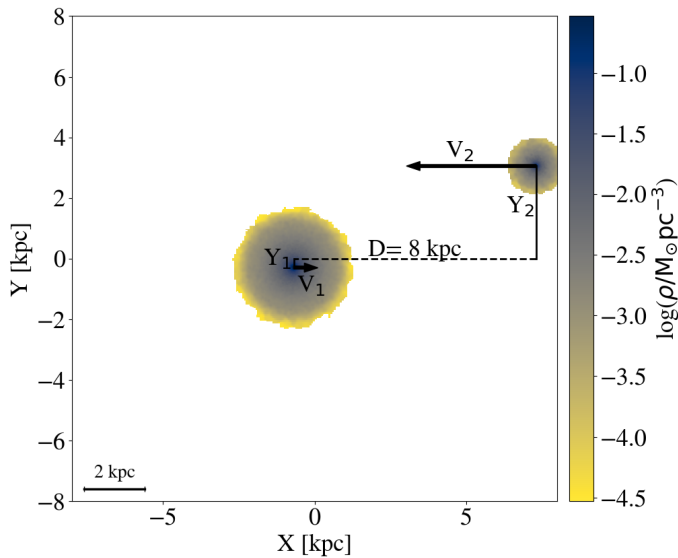


Fig. 2: Example of merger initial conditions prepared with DICE (see Sec. 2.1.4). The density map in the X-Y plane shows the total (dark matter+stars) density ( $\rho$ ) which has been mass averaged along the Z-axis. The two progenitors are placed in the simulation box at a distance  $D = 8$  kpc along the X-axis and with an impact parameter  $|Y_1| + |Y_2|$  (eq.s 5b). The arrows mark the direction of the initial velocity of each progenitor (eq. 5c).

tion of the progenitors can be written as

$$X_{1,2} = \mp D \frac{M_{2,1}}{M_1 + M_2}, \quad (5a)$$

$$Y_{1,2} = \mp \frac{l}{|V_1| + |V_2|} \frac{M_1 + M_2}{M_{1,2}}, \quad (5b)$$

with their velocity along the x-axis being

$$V_{1,2} = \pm \sqrt{2k \frac{M_{2,1}}{M_{1,2}}}. \quad (5c)$$

In eq.s 5,  $M_i$  is the total mass of the  $i$ th progenitor, i.e.,  $M_i = M_{i,DM} + M_{i,*}$ ;  $l$  is the specific angular momentum (w.r.t. the center of mass)

$$l = \frac{\sum_s m_s \mathbf{v}_s \times \mathbf{x}_s}{\sum_s m_s}, \quad (6a)$$

where the sum over  $s$  is extended to all particles, and  $k$  is the specific kinetic energy

$$k = \frac{\sum_s m_s v_s^2}{\sum_s m_s}. \quad (6b)$$

We varied the values of  $l$  and  $k$  to probe different merging trajectories. Fig. 2 shows an example of the merger's initial conditions, in which the two progenitors have total masses  $M_1 = 4.8 \times 10^7 M_\odot$  and  $M_2 = 4.6 \times 10^6 M_\odot$ , the specific merger kinetic energy is  $k = 0.72 \text{ pc}^2 \text{ Myr}^{-2}$ , and the angular momentum is  $l = 1.1 \times 10^3 \text{ pc}^2 \text{ Myr}^{-1}$ .

## 2.2. Parameterization of the merger

We focus our exploration on the five parameters: the merger mass ratio  $M_1/M_2$ , the dark matter content  $M_{DM}/M_*$ , the stellar

Table 1: Summary of the parameters adopted in the suite:  $M_1/M_2$  is the merger mass ratio,  $M_{DM}/M_*$  is the halo to stellar mass ratio,  $R_{1/2}$  is the half-mass radius of the more massive progenitor (progenitor 1, eq. 4), while  $l$  and  $k$  are the specific merger angular momentum and the specific merger kinetic energy, respectively. For each parameter, we indicate the minimum and maximum of the value adopted in the sampling (eq. 9)

parameter	min	max	unit	definition
$M_1/M_2$	1	30	-	Sec. 2.2.1
$M_{DM}/M_*$	$8 \times 10^3$	$10^5$	-	Sec. 2.2.2
$R_{1/2}$	15	150	pc	Sec. 2.2.3, eq. 4
$l$	$10^2$	$3 \times 10^3$	$\frac{\text{pc}^2}{\text{Myr}}$	Sec. 2.2.4, eq. 6a
$k$	0.1	3	$\frac{\text{pc}^2}{\text{Myr}^2}$	Sec. 2.2.4, eq. 6b

radius of the progenitors  $R_{1/2}$ , the specific angular momentum  $l$ , and the specific kinetic energy  $k$ . In the following, we first describe the interval explored for each of these properties and then present how we explore the parameter space via a Latin Hypercube sampling. Table 1 summarizes the properties and relative intervals explored.

### 2.2.1. Merger mass ratio

Defining the merger mass ratio between the two progenitors as  $M_1/M_2$ , we note that previous works (e.g., Deason et al. 2022) identify a peak in the fraction of stars in the stellar halo when  $M_1/M_2 \approx 5$ . Therefore, to fully capture its dependency in UFD mergers, we explored the interval  $M_1/M_2 \in [1, 30]$ .

It is convenient to use the merger mass ratio to define the stellar mass of each progenitor:

$$M_{1,*} = M_{tot,*} \frac{M_1/M_2}{1 + M_1/M_2} \quad (7a)$$

$$M_{2,*} = M_{tot,*} \frac{1}{1 + M_1/M_2}, \quad (7b)$$

where  $M_{tot,*} = M_{1,*} + M_{2,*}$  is the total stellar mass in the simulation, which is set to  $M_{tot,*} = 6 \times 10^3 M_\odot$  to ensure that, even in the case of stellar mass loss during the merger, the post-merging galaxy stellar mass is consistent with Tucana II estimations  $M_*^{\text{TucII}} = 3_{-2}^{+7} \times 10^3 M_\odot$  (Bechtol et al. 2015).

### 2.2.2. Dark matter to stellar mass ratio

The dark matter content of UFDs is poorly constrained. Velocity dispersion observations can determine the dark matter mass within the luminous part of the galaxy, however, extrapolating the total halo masses from such a measurement is an uncertain endeavor (e.g., Errani et al. 2018). For this reason, we explored an interval of values of  $M_{DM}$ , investigating whether the dark matter abundance impacts the stellar halo formation. To this end, we varied the stellar to dark matter mass ratio  $M_{DM}/M_*$ , which determines the dark matter mass of each progenitor once the merger mass ratio sets the stellar mass.

The interval explored is  $M_{DM}/M_* \in [8, 100] \times 10^3$ , and, in Fig. 3, we report it in an  $M_* - M_{DM}$  plane with a shaded region. The selected range includes the latest dark matter mass estimate within 1 kpc for Tucana II,  $M_{DM}^{\text{TucII}} \sim 2.5 \times 10^7 M_\odot$  (Chiti et al. 2021). Further, the explored range roughly brackets the predictions by abundance-matching methods (Behroozi et al. 2013) for galaxies between  $z = 6$  and  $z = 0$  (green lines in Fig. 3). In the

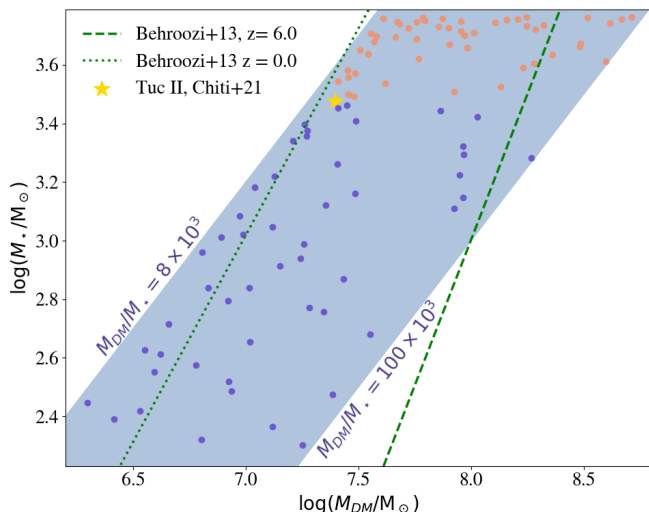


Fig. 3: Parameter sampling in the Dark matter ( $M_{\text{DM}}$ ) vs stellar mass ( $M_{\star}$ ) plane. Each blue (orange) point represents the least (more) massive progenitor in a merging simulation. The shaded region indicates the dark matter to stellar mass ( $M_{\text{DM}}/M_{\star}$ ) interval explored by the suite. The gold star shows the estimate of Tucana II from Chiti et al. (2021) observations, while the green lines are the extrapolation from the abundance matching model from Behroozi et al. (2013) at redshift  $z = 0$  and 6.

plot, each point represents a progenitor in our simulation suite (see Sec. 2.2 for the sampling), with orange (blue) indicating the more (least) massive progenitor.

### 2.2.3. Half-mass radius

Observations show that UFDs with a stellar mass similar to Tucana II have a half-light radius, i.e., the radius that contains half of the galaxy’s luminosity, ranging from tens to hundreds of parsecs (Simon 2019). The half-light radius is equal to the half-mass radius, assuming a constant luminosity-to-mass ratio, and thus, we decide to explore an interval of values  $R_{1/2} \in [15, 150]$  pc.

We assign the value of  $R_{1/2}$  to the more massive progenitor, and we define the mean stellar density as

$$\bar{\rho}_{\star} = \frac{3}{8\pi} \frac{M_{1,\star}}{R_{1/2}^3}. \quad (8)$$

To set the scale radius of the other progenitor, we impose that the two galaxies have the same  $\bar{\rho}_{\star}$ . This approach prevents us from exploring the dependency of the stellar halo formation on the density difference between the two progenitors, however, by avoiding double sampling the  $R_{1/2}$  parameter, we reduce the number of dimensions explored, thus strengthening the results of our exploration.

### 2.2.4. Specific angular momentum and kinetic energy

Since we want to study the merging event between galaxies, we limit our explorations to values of  $l$  and  $k$  that are highly likely to produce the merging of the two progenitors. Specifically, the intervals explored are  $l \in [100, 3000] \text{ pc}^2 \text{ Myr}^{-1}$  and  $k \in [0.1, 3] \text{ pc}^2 \text{ Myr}^{-2}$ . We adopt these intervals after testing them with (i) the solution of the two-body problem, assuming

both galaxies as point masses, and (ii) a low-resolution version of the simulation suite, as further explained in the following.

### 2.3. Parameter space sampling

Sampling the parameter space is a delicate endeavor. The more samples we have, the finer we explore the parameter space with increasing computational cost. We use a five-dimensional Latin hypercube sampling (McKay et al. 1979) to maximize the exploration while keeping the number of samples/simulations low. The implemented sampling consists of 47 nodes, i.e., sampled points, with each node being a unique set of the five parameters defining the merger, i.e.,

$$\kappa = (l, k, M_1/M_2, M_{\text{DM}}/M_{\star}, R_{1/2}). \quad (9)$$

To compute the node values with the LHS prescription, we divide the range of each individual parameter into a set of equally probable intervals and the algorithm selects one sample from each interval, ensuring that the samples are evenly spaced out across the entire range. We adopt a logarithmic scaling for the five components in the node  $\kappa$ .

We verify that the progenitors are on merging trajectories before evolving the initial conditions generated by the 47 nodes at full resolution. To do so, we generate the initial conditions at lower dark matter resolution, i.e.,  $m_{\text{DM}}^{\text{low}} = 10^3 M_{\odot}$  and evolve them. The coarser resolution makes these simulations run at around a tenth of the computational cost, enabling us to evolve each one for 5 Gyr and check whether or not the progenitors merge. In addition, having the same initial conditions simulated using two different resolutions allows us to evaluate the resolution effects, as detailed in App. A.

### 2.4. Time evolution

We use the public version of the moving-mesh hydrodynamic code AREPO (Springel 2010; Weinberger et al. 2020) to evolve the initial conditions. AREPO performs the time evolution with a second-order accurate leapfrog scheme, using a Tree-Particle-Mesh (Tree-PM) method (Bagla 2002) to compute the gravitational interaction between particles. Having solely two galaxies in the simulation box, we adopt only the oct-tree grouping scheme (Barnes & Hut 1986) for the force evaluation, using non-periodic boundary conditions. The gravitational softening length of dark matter and stellar particles is  $\epsilon = 1$  pc, and the simulation box has side  $L = 100$  kpc.

Each simulation evolves until the two progenitors merge into a single virialized galaxy. We use the on-the-fly friends-of-friends group finder (FoF) available within AREPO and originally described in Springel et al. (2001) to identify the merging instant. The algorithm groups together particles that are at a distance less than 0.2 times the mean inter-particle separation. We define the merging instant as the point at which the FoF algorithm finds a single galaxy.

### 2.5. Merger emulator

Having a high computational cost is a common limitation in numerical simulations, especially when a parameter space exploration is involved; a possible solution is the implementation of an *emulator*, to either reduce the number of simulations needed (e.g., Bird et al. 2019; Rogers et al. 2019; Brown et al. 2024) or to speed up the computation (e.g., Spurio Mancini et al. 2022; Branca & Pallottini 2024; Robinson et al. 2024; Bartlett et al.

2024). In this work, we adopt a neural network (NN) as an emulator to enhance the parameter space exploration. The NN approximates a function that, taking the merger configuration and progenitor initial conditions as input, returns the properties of the post-merger galaxy without requiring new simulations. Indeed, thanks to the Universal Approximation Theorem (UAT, Cybenko 1989), a trained NN can approximate with arbitrary precision the non-linear function that maps the input parameters,  $\kappa$ , into outputs characterizing the galaxy and the stellar halo. For the present work, we set two outputs

$$(R_\star, f_5) = \text{NN}(\kappa), \quad (10)$$

where with  $R_\star$  we refer to the half-mass radius of the post-merger galaxy to distinguish it from the massive progenitor's half-mass radius  $R_{1/2}$  which is one of the inputs of the NN;  $f_5$  is the stellar halo mass fraction, i.e., the fraction of stars at  $r > 5R_\star$ . Such a choice of outputs enables us to directly compare our results with Tucana II observations (see later Sec.s 3.2 and 3.3).

We adopt a regularized loss function to prevent overfitting and train the emulator on the simulation outputs. The number of training points is small compared to the dimensionality of the problem and we overcome the sparse sampling issue by adopting a Latin Hypercube sampling (see Sec. ??), which ensures uniform coverage of the parameter space. Furthermore, deep NNs are relatively unaffected by the growing difficulty of analyzing data as the number of dimensions increases, i.e., the ‘‘curse of dimensionality’’, when approximating compositional functions (Poggio & Liao 2018). We refer to App. B for a complete description of the NN.

### 3. Results

First, we present the evolution of a single simulation and its analysis to overview the merging process (Sec. 3.1). Then, we repeat the same analysis on all the simulations, use the results to train the emulator, and explore the parameter space to determine the dependency of the stellar halo on the initial conditions (Sec. 3.2). Finally, we directly compare our findings with the observations of Tucana II (Sec. 3.3).

#### 3.1. Merging of UFDs: an overview

To showcase the merging process, we select simulation SIM\_47, which produces a post-merger galaxy with a stellar surface density consistent with the one observed in Tucana II, see Sec 3.3. Simulation SIM\_47 has merger mass ratio  $M_1/M_2 \approx 10$ , scale radius  $R_{1/2} \approx 120$  pc, mass-to-light ratio  $M_{\text{DM}}/M_\star \approx 10^4$ , specific angular momentum  $l \approx 1.1 \times 10^3 \text{ pc}^2 \text{ Myr}^{-1}$ , and specific kinetic energy  $k \approx 0.72 \text{ pc}^2 \text{ Myr}^{-2}$ . Note that this is the set of parameters already used in Figs 1 and 2, which show the initial conditions and merger setup, respectively.

To visualize the spatial evolution in the simulated volume, we report the stellar surface density for the various phases of the merger in Fig. 4. The top left panel is at  $t = 0.2$  Gyr when the two progenitors are virialized. The top right panel shows the gravitational interaction between the two progenitors during the third and last passage before merger completion. The bottom panels are at  $t = 4.01$  Gyr when the post-merger galaxy is virialized. The effect of the merger on the morphology of the galaxy is evident when comparing the post-merger galaxy with one of its progenitors, the right panel in Fig. 1. To help the comparison, we mark 1, 3, and  $5R_\star$  in both panels of Fig. 1 and Fig. 4. The progenitor is mostly contained within  $5R_{1/2}$ , while the post-merger

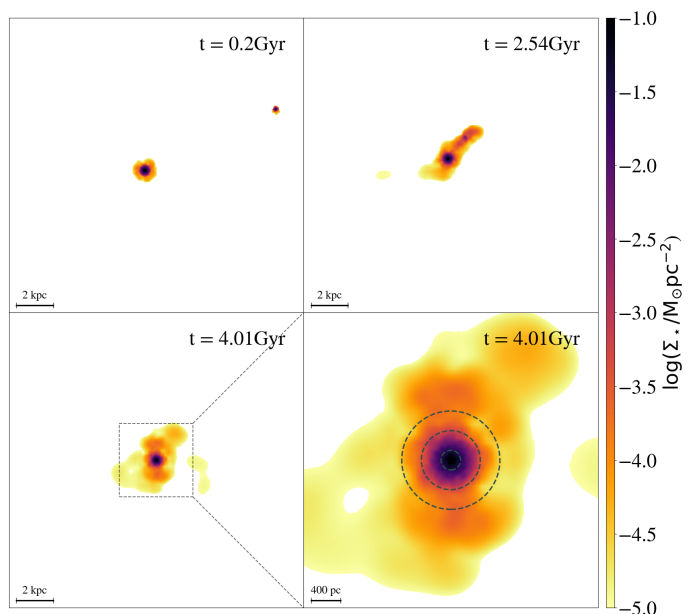


Fig. 4: Example of merger evolution. The different panels report the stellar surface density ( $\Sigma_\star$ ) maps at various evolutionary stages for progenitors with  $M_1/M_2 \approx 10$  (profile in Fig. 1) and the merger setup in Fig. 2. The bottom right panel is a zoom-in on the virialized post-merger galaxy, and the three dashed circles have radii one, three, and five half-mass radii. After the merging, the resulting fraction of stars in the outskirts is  $f_5 \sim 5.5\%$ .

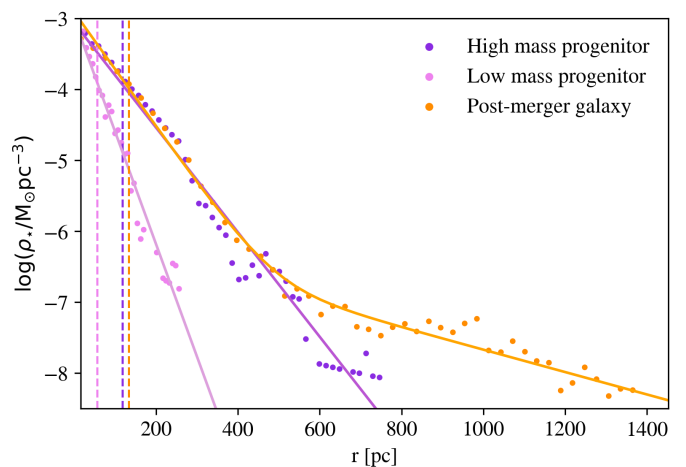


Fig. 5: Example of pre- vs post-merging stellar distributions. We show the profile for the simulation selected for Fig. 4 by reporting  $\rho_\star$  for the two progenitors with shades of purple and the post-merger galaxy in orange. The solid lines are the fitted profile, which is exponential (eq. 4) and a sum of exponential for the progenitors and the post-merger galaxy, respectively. The vertical lines mark the half-mass radius for each galaxy.

galaxy is wider, extending way beyond  $5R_\star$ . The extended stellar distribution at large radii, i.e., the stellar halo, forms as a result of the merger event and is bar-shaped. Therefore, contrary to the progenitors, the post-merger galaxy is asymmetric and we account for the asymmetry using an ensemble average<sup>2</sup> to estimate

<sup>2</sup> We consider all possible projection planes, take the median as  $R_{1/2}$  and the 16-th and 84-th percentiles as the error.

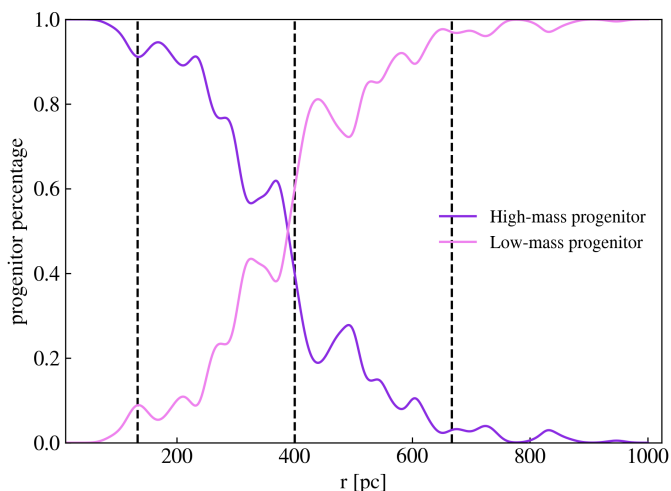


Fig. 6: Origin of the stars in the post-merger galaxy. For the simulation selected for Fig. 5, we show the radial distribution of the fraction of stars that originally belonged to the high-mass progenitor (purple) and the low-mass progenitor (pink). The dashed vertical lines are at 1, 3, and 5  $R_*$ .

$R_*$ , which we recall is the half-mass radius of the 2D projection of the galaxy.

To analyze the difference between pre- and post-merger galaxies’ stellar distribution, in Fig. 5 we compare the stellar density of the two progenitors (shades of purple) and the post-merger galaxy (orange). The vertical lines are the half-mass radius for each galaxy, while the solid lines are the fitted profiles: exponential (eq. 4) for both progenitors and the sum of two exponential profiles for the post-merger galaxy. The double exponential profile models the formation of a dense core and a sparse stellar halo and better fits the post-merger stellar distribution. The difference between the post-merger galaxy and its massive progenitor stellar distribution lies in the outskirts, where the post-merger galaxy has a higher mass fraction due to the formation of a stellar halo. The higher mass fraction affects the half-mass radius, going from  $R_{1/2} = (114 \pm 1)$  pc of the massive progenitor to  $R_* = 130^{+3}_{-1}$  pc of the post-merger galaxy. The error distribution in  $R_*$  is due to the asymmetry of the stellar halo formed via a merger.

Tidal interactions during the merger strip stars from the less massive progenitor and form the stellar halo, as shown in Fig. 6, where we report the fraction of stars of the post-merger galaxy coming from each progenitor at different radii. We adopted the same progenitor colors of Fig. 5, and the dashed lines are at 1, 3, and 5  $R_*$ . While the center of the post-merger galaxy is dominated by stars of the more massive progenitor, beyond 3  $R_*$  the majority of the stars come from the smaller progenitor. This distribution shows that stars of the low mass progenitor compose the stellar halo, and this is key to understanding the trends we observe exploring the parameter space, Sec. 3.2.

To quantify the presence of a stellar halo, we follow Tarumi et al. (2021) and calculate  $f_5$ , which we recall is the fraction of stars beyond 5  $R_{1/2}$ . Since  $f_5$  depends on the half-mass radius, we perform the same ensemble average considering all possible projection planes. For each projection plane, we randomly sample the stellar surface density distribution using the same number of stars of Chiti et al. (2021), i.e., 19 stars, and consider the mean and standard deviation as  $f_5$  and its error. We estimate  $f_5 = 0.16 \pm 0.4\%$  and  $f_5 = 0.19 \pm 0.03\%$  for the

two progenitors. These values are consistent with the ones expected in isolated galaxies with an exponential profile, where  $f_5$  tends to zero. Fig. 4 shows the formation of a stellar halo after the merger, and as a result of the stellar halo formation, the fraction of outskirts stars in the post-merger galaxy increases to  $f_5 = 5.4 \pm 1.8\%$ . For comparison, the observed value in Tucana II is  $f_5^{\text{TucII}} = 2/19 = 10.5\%$ .

### 3.2. Exploration of the parameter space with the emulator

Using the radius  $R_*$  and the fraction of stars in the outskirts  $f_5$  of each post-merger galaxy, we build the dataset to train the emulator. Recall that (Sec. 2.5) the input values of the emulator are the explored initial parameters,  $l$ ,  $k$ ,  $M_1/M_2$ ,  $M_{\text{DM}}/M_*$ , and  $R_{1/2}$ , and the output values are the median of the two post-merger quantities  $f_5$  and  $R_*$  (see eq. 10). For details of the NN architecture and its training, we refer to App. B.

Fig. 7 shows the distribution of the emulated outputs ( $f_5$  top row,  $R_*$  bottom row) of  $10^6$  different initial conditions (IC) log-spaced distributed. The orange dots represent the results of the training simulations, and their overlap with the emulated results confirms the emulator’s robustness. The last column of Fig. 7 shows the distribution of output values in the parameter space explored. The distribution of  $f_5$  peaks around 5%, the value found by Tarumi et al. (2021) for their *dry* merger. The  $R_*$  distribution increases at low values. This trend is primarily due to the distribution of the training data, which is affected by numerical heating at low  $R_{1/2}$ , as explained in detail in the App. A. Consequently, the emulator predicts a higher frequency of galaxies with low  $R_*$  due to the higher number of simulations with  $R_* \approx 40$  pc.

The red-shaded areas are the observed values for Tucana II with the relative error. As the radius, we adopt  $R_{1/2}^{\text{TucII}} = (120 \pm 30)$  pc (Bechtol et al. 2015), while we compute the fraction of distant stars  $f_5^{\text{TucII}} = 10 \pm 5\%$  from the distribution of individual stars observed in Chiti et al. (2021). The error assigned to  $f_5$  considers that one of the two stars in the outskirts can lie within 5  $R_{1/2}$ , thus changing the fraction to 5%.

The emulated results, whose median is given by the gold line, show little to no dependency on the specific angular momentum  $l$ , kinetic energy  $k$ , and dark matter content  $M_{\text{DM}}/M_*$ . Clear trends are instead present for the merger mass ratio  $M_1/M_2$  and the progenitor half-mass radius  $R_{1/2}$ ; specifically,  $R_*$  correlates almost linearly with  $R_{1/2}$  while  $f_5$  increases with  $M_1/M_2$ , peaks around  $M_1/M_2 \approx 6$ , and then decreases. The correlation between the sizes of the progenitor and the post-merger galaxy is expected, since the larger the progenitor is, the larger the post-merger galaxy will be. Meanwhile, the correlation between  $f_5$  and the merger mass ratio emerges because, as discussed in Sec. 3.1, the stellar halo stars primarily originate from the less massive progenitor (the “satellite”), leading to two distinct regimes. When the two progenitors have comparable masses, they mix, forming a post-merger galaxy with a minimal stellar halo and a small  $f_5$ . In this regime, increasing the merger mass ratio weakens the depth of the potential well of the satellite, making it easier for its stars to be stripped during the merger and form a more prominent stellar halo. As a result,  $f_5$  initially increases with the  $M_1/M_2$  ratio. However, increasing  $M_1/M_2$  reduces the number of stars in the “satellite”, leading to a decrease in the number of available stars to form the stellar halo. For this reason, beyond a certain threshold (approximately  $M_1/M_2 \approx 6$ ),  $f_5$  begins to decline.

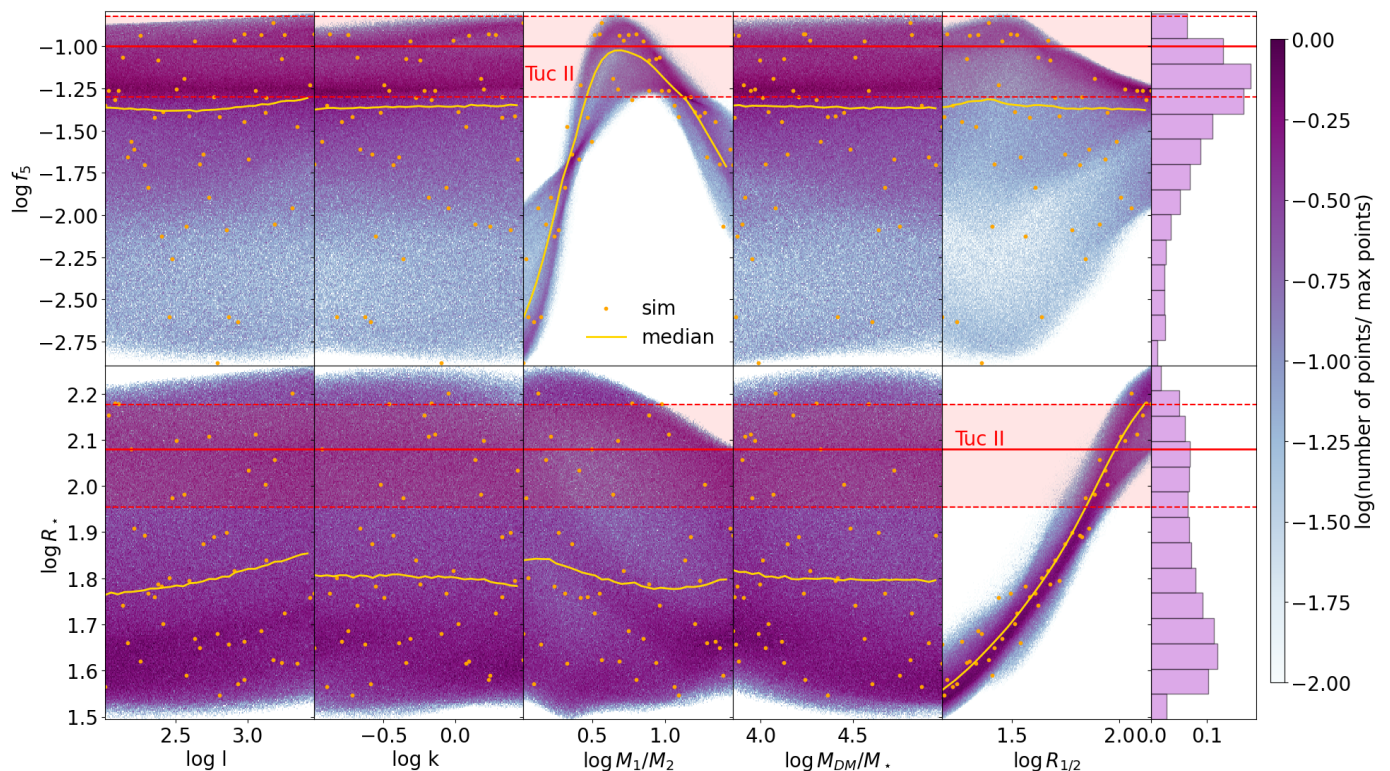


Fig. 7: Emulation of the post-merging  $f_5$  (upper panels) and stellar radius ( $R_*$ , lower panels) as a function of merger setup parameters, i.e., specific angular momentum ( $l$ , eq. 6a), specific kinetic energy ( $k$ , eq. 6b), mass ratio ( $M_1/M_2$ ), dark to stellar mass ratio ( $M_{DM}/M_*$ ), and pre-merger stellar size ( $R_{1/2}$ , 4). Each of the first five columns gives the distribution of outputs of the merging process as a function of a single parameter. The distribution is obtained by emulating  $10^6$  IC log-spaced distributed (see Tab. 1), and the gold line represents its median. The orange points are the individual simulations used to train the emulator. The red line (shaded region) gives the average (dispersion) of the observed values for Tucana II (Bechtol et al. 2015; Chiti et al. 2021). The last column shows the distribution of the emulated output normalized to the total number of inferences.

To quantify the dependencies of  $f_5$  and  $R_*$  from the initial conditions ( $\kappa$ ), we performed a principal component analysis (PCA). A PCA studies the linear transformation (component) of the parameter space of the data. Such components are ranked such that the variance is decreasing. Thus, the first (principal) components can explain most of the variation of the original data set. We perform the PCA separately for the two outputs, i.e., one for ( $f_5, \kappa$ ) and one for ( $R_*, \kappa$ ). For each PCA, we consider  $10^6$  points in six dimensions, normalizing each dimension such that its mean and standard deviation are 0 and 1, respectively. The first PCA component for  $f_5$  ( $R_*$ ) is dominated by  $f_5$  ( $R_*$ ) and  $M_1/M_2$  ( $R_{1/2}$ ), confirming the trends observed in Fig. 7.

To determine the secondary dependencies, we perform two additional PCAs considering a reduced number of points. Specifically, when analyzing  $f_5$ , we consider the points with  $M_1/M_2 \in [5, 7]$ , i.e., where  $f_5$  peaks, while for  $R_*$ , we consider the points with the progenitor radius  $R_{1/2} \in [90, 110]$  pc, i.e., the progenitor radius producing a post-merger galaxy radius consistent with Tucana II observations. The first reduced PCA component for  $f_5$  ( $R_*$ ) is dominated by  $f_5$  ( $R_*$ ) and  $R_{1/2}$  ( $M_1/M_2$ ), revealing that the principal dependency of one output is the secondary dependency of the other.

Once we remove the dependency on  $M_1/M_2$  and  $R_{1/2}$ , selecting points simultaneously in the intervals  $M_1/M_2 \in [5, 7]$  and  $R_{1/2} \in [125, 145]$  pc, we notice that  $f_5$  and  $R_*$  marginally depend on the other three parameters  $l$ ,  $k$ ,  $M_{DM}/M_*$ . The relative importance depends on the intervals considered, but generally,  $M_{DM}/M_*$  is the least important for both  $f_5$  and  $R_*$ .

### 3.3. Comparison with Tucana II observations

We can now compare the emulated  $f_5$  and  $R_*$  with the observations to infer the properties of Tucana II progenitors. As described in Sec. 3.2, we adopted  $R_{1/2}^{\text{TucII}} = (120 \pm 30)$  pc and  $f_5^{\text{TucII}} = 10 \pm 5\%$  as observed values of half-mass radius and fraction of stellar halo stars in Tucana II, respectively.

Fig. 8 shows the distribution of the output values consistent with Tucana II observations, and based on the PCA results, we limit the study to two initial parameters that define the output values, i.e.,  $M_1/M_2$  and  $R_{1/2}$ . The top row shows the distribution of these initial parameters, with the dashed lines indicating the median and 16-th and 84-th percentiles, while the four orange points represent four simulations in the suite consistent with Tucana II observations. Consistency with observations is achieved for initial conditions with progenitor half-mass radius  $R_{1/2} = 97_{-18}^{+25}$  pc and merger mass ratio  $M_1/M_2 = 8_{-3}^{+4}$ . Therefore, we determine that an intermediate merger ( $5 < M_1/M_2 < 12$ ) forms a stellar halo like the one observed for Tucana II. Such a finding is consistent with Deason et al. (2014), which report that 40% of  $z = 0$  UFDs in their simulations experienced at least one major merger in the last 12 Gyr. Among the four post-merger simulations consistent with observations, SIM\_41 and SIM\_47 are consistent within  $1.1\sigma$  from<sup>3</sup> the inferred values of  $M_1/M_2$  and  $R_{1/2}$ , SIM\_17 has a progenitor radius slightly larger, i.e.,

<sup>3</sup> For the results of our models, the left (right)  $\sigma$  is defined as the interval between the 16-th (84-th) percentile and the median. Different defi-



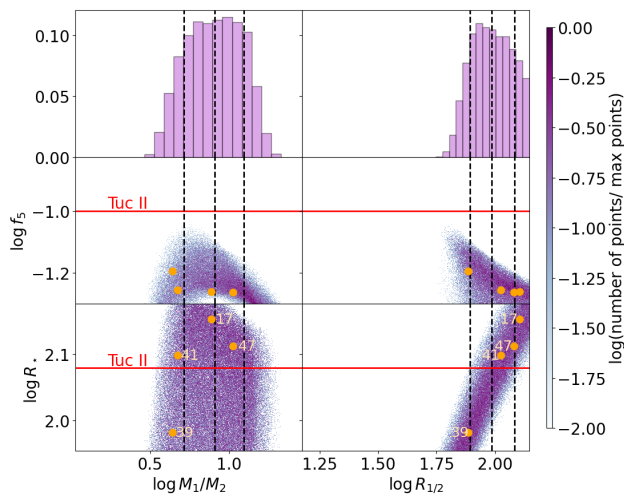


Fig. 8: Distributions of the input couple  $R_{1/2}$  and  $M_1/M_2$  that give  $f_5$  and  $R_*$  simultaneously consistent with the observations from Tucana II. Similarly to Fig. 7, the red line gives the average value inferred from observations, but the ranges for  $f_5$  and  $R_*$  are cut to include only the observational uncertainty, i.e.,  $f_5^{\text{TucII}} = 10 \pm 5\%$  (Chiti et al. 2021) and  $R_{1/2}^{\text{TucII}} = (120 \pm 30)$  pc (Bechtol et al. 2015), respectively. The orange points are the post-merger galaxies consistent with observations from Tucana II, and are numbered with their simulation ID.

$> 1.1\sigma$ , and SIM\_39 has both  $M_1/M_2$  and  $R_{1/2}$  values  $> 1.1\sigma$ . We note that the errors on the inferred properties highly depend on the value and error adopted for  $f_5$ , and better constraining it helps in decreasing the uncertainties on  $M_1/M_2$  and  $R_{1/2}$ . For example, lowering  $f_5$  error by a factor 2, i.e.,  $\sim \pm 2.5\%$ , results in a decrease of a factor 3 on the error of the initial conditions consistent with Tucana II.

One method to reduce the error on  $f_5$  is to increase the number of identified stars, for example, using Gaia data. In recent work, Jensen et al. (2024) exploit Gaia data employing a selection algorithm based on spatial, color-magnitude, and proper motion information targeting low brightness features of Milky Way dwarf satellites. They are able to identify the second low-density outer profile of nine satellites, including Tucana II, and for each of them, derive the stellar surface density profile. They model it as the sum of two exponential profiles, i.e.,

$$\Sigma(r) = \Sigma_0 \left( e^{-r/r_e} + B e^{-r/r_s} \right), \quad (11)$$

where  $\Sigma_0$  is the central surface density,  $r_e$  is the exponential scale radius,  $B$  is the normalization of the outer component ( $0 \leq B \leq 1$ ), and  $r_s$  the scale radius of the outer component ( $1.68r_s > R_{1/2}$ ). They derive  $r_e$  from the literature value of the half-light radius such that  $R_{1/2} = 1.68r_e$ . Unfortunately, we cannot use their star candidates list to evaluate  $f_5$ , since there are no spectroscopic follow-ups to verify the membership of each star. However, we can test our results by comparing the surface density of our simulated post-merger galaxies with the one derived by them.

Fig. 9 shows the derived stellar surface density profile of Tucana II (green) and our simulated post-merger galaxies (orange), and each of the four columns refers to a simulation that is simultaneously consistent with the observed values of  $f_5$  and  $R_{1/2}$ . As

nitions of  $\sigma$  give slight quantitative differences, but the physical picture is unchanged.

we can see, most of these four simulations reasonably match the observed stellar halo well beyond 1 kpc and only SIM\_39 is not consistent with the observed data. We quantify the accordance between simulations and observations using the standard  $\chi^2$  procedure:

$$\chi^2 = \sum_{i=1}^{10} \frac{(\Sigma_{i,obs} - \Sigma_{i,sim})^2}{\sigma_{i,obs}^2 + \sigma_{i,sim}^2}, \quad (12)$$

where  $\Sigma_{i,obs}$  ( $\sigma_{i,obs}$ ) and  $\Sigma_{i,sim}$  ( $\sigma_{i,sim}$ ) are the stellar surface density profiles (standard errors) derived from observations and simulations, respectively. We use ten radius bins to be consistent with Jensen et al. (2024), and for each bin, we compute  $\sigma_{i,obs}$  propagating  $R_{1/2}$ ,  $B$ , and  $r_s$  errors, and we compute  $\sigma_{i,sim}$  as the Poisson error. The three simulations within  $1.1\sigma$  from the inferred  $M_1/M_2$ , i.e., SIM\_17, SIM\_41, and SIM\_47, have a good agreement, i.e.,  $\chi^2 = 0.5 - 2$ . Note that  $\chi^2$  of SIM\_17 is larger, since the accordance with  $R_{1/2}$  is worse. All three simulation show the two-component profiles with differences in the central density  $\Sigma_0$  and the transition to the second exponential profile. Their initial conditions span almost all the angular momentum values, confirming that the formation of a stellar halo does not depend on angular momentum in the interval explored in this work. We recall that we consider  $l$  values that result in a merger between the two progenitors. For SIM\_39, the surface density significantly diverges from the observed one ( $\chi^2 = 12.0$ ). Although the fraction of distant stars is consistent with observations,  $f_5 = 6.4^{+2}_{-4}$ , the simulation features an inner core that is  $2\times$  denser and  $0.5\times$  smaller compared to observations. This is due to the offset from  $M_1/M_2$  and  $R_{1/2}$ , that are at  $> 1.1\sigma$  from the emulator predictions.

#### 4. Summary and Discussion

In this work, we investigate merger events as the formation scenario of stellar halos around Ultra-Faint dwarf galaxies (UFDs). We study the impact of different merger and progenitor properties and focus on reproducing the stellar halo observed in Tucana II by Chiti et al. (2021, 2023); Jensen et al. (2024).

To this end, we developed a suite of 47 N-body simulations of isolated *dry* mergers between two idealized progenitors of Tucana II with a stellar resolution of a single solar mass. We use DICE (Perret 2016) to generate the initial conditions, assuming an exponential profile for the stellar component of both progenitors, and AREPO (Weinberger et al. 2020) to evolve the simulation until the post-merger galaxy virializes. The suite explores different merger trajectories and progenitors properties, assigning to each simulation a unique set of five parameters: i) the specific angular momentum  $l$ , ii) the specific kinetic energy  $k$ , iii) the merger mass ratio  $M_1/M_2$ , iv) the dark matter content  $M_{DM}/M_*$ , and v) the half-mass radius of the more massive progenitor  $R_{1/2}$ . For each post-merger galaxy, we quantify the formation of a stellar halo using two properties: the half-mass radius  $R_*$ , and the fraction of stars  $f_5$  at high radii ( $> 5R_*$ ).

We develop a neural network-based emulator to avoid the extreme computational cost expected from a high-resolution sampling of the selected 5-dimension parameter space. Via the emulator, we quickly obtain the properties of one million post-merger galaxies, i.e.,  $R_*$  and  $f_5$ , and study the dependency of the stellar halo formation on the initial conditions of the merger and progenitors. By comparing the emulated properties to Tucana II observations, we infer consistent merger and progenitor characteristics. Additionally, we compare the stellar surface density of simulated post-merger galaxies and Tucana II to further validate the merger scenario.

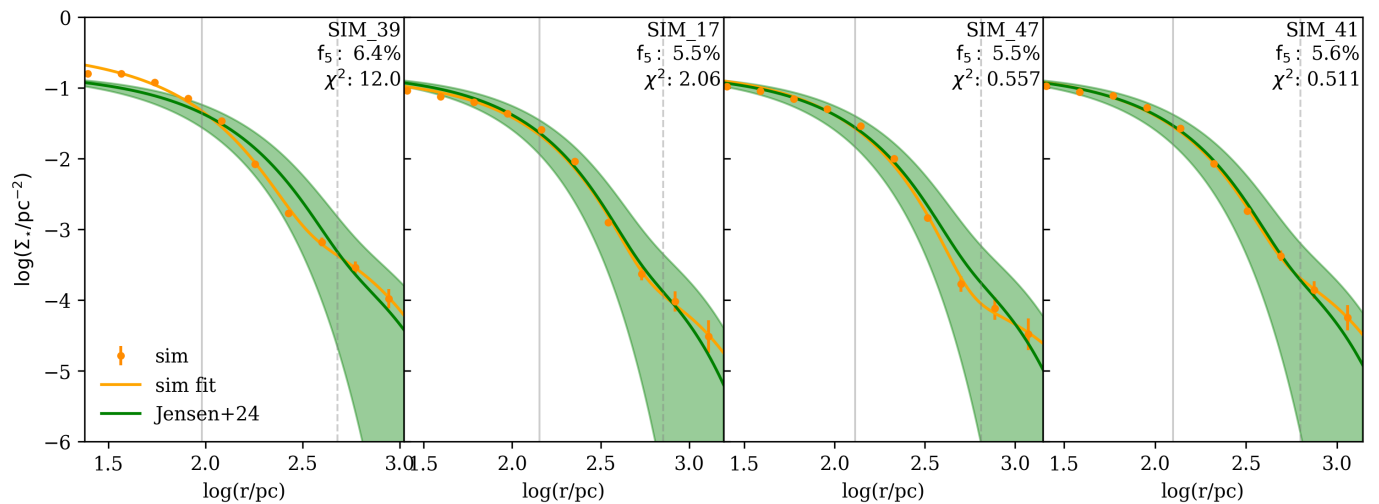


Fig. 9: Comparison of the observed stellar number density distribution of Tucana II and the simulations with the  $f_5$  and  $R_{1/2}$  parameters closest to the observed values ( $f_5^{\text{TucII}} = 10 \pm 5\%$  from Chiti et al. 2021 and  $R_{1/2}^{\text{TucII}}/\text{pc} = 120 \pm 30$  from Bechtol et al. 2015). Each panel shows a different simulation, as indicated in the inset, ordered by decreasing  $\chi^2$  value. The green line (shaded area) gives the mode (error) of the profile for Tucana II, as observed by Jensen et al. (2024). The orange line (points with bars) gives the best fit (average and s.t.d of the data points) of the profile of a simulated post-merger galaxy, obtained by adopting a two-exponential profile (eq. 11). The gray solid (dashed) line shows the  $R_*$  ( $5 R_*$ ) post-merger radius.

We can summarize our most important results as follows:

- The merger mass ratio  $M_1/M_2$  (progenitors' size  $R_{1/2}$ ) drives the formation of a stellar halo  $f_5$  (the size of the galaxy  $R_*$ ) in the aftermath of a merger, with the progenitors' size  $R_{1/2}$  (merger mass ratio  $M_1/M_2$ ) being the secondary dependency. In the interval explored, the specific angular momentum  $l$ , specific kinetic energy  $k$ , and dark matter abundance  $M_{\text{DM}}/M_*$  have a negligible impact on both the stellar halo formation and the size of the post-merger galaxy.
- Using the observed fraction of distant stars,  $f_5^{\text{TucII}} = 10.5\%$  (Chiti et al. 2021), and half-light radius  $R_*^{\text{TucII}} = 120$  pc (Bechtol et al. 2015) of Tucana II, we predict that the merger mass ratio and massive progenitor size consistent with observations are  $M_1/M_2 = 8^{+4}_{-3}$  and  $R_{1/2} = 97^{+25}_{-18}$  pc. The merger that can form Tucana II's stellar halo is intermediate, while the size of present-day Tucana II is similar to the radius of its massive progenitor.
- Four simulated post-merger galaxies are consistent with  $f_5^{\text{TucII}}$  and  $R_*^{\text{TucII}}$ . Three simulations have  $M_1/M_2$  ( $R_{1/2}$ ) within  $1.1\sigma$  ( $1.2\sigma$ ) from the predicted values: their stellar surface density well reproduce ( $\chi^2 \approx 0.5 - 2$ ) the one observed (Jensen et al. 2024). The simulation with both  $M_1/M_2$  and  $R_{1/2}$  at  $> 1.2\sigma$  from the predictions deviates the most from observations ( $\chi^2 = 12$ ). This underlines the importance of  $M_1/M_2$  and  $R_{1/2}$  in determining the post-merger galaxy morphology.

Our results confirm previous findings about the importance of the merger mass ratio on the formation of a stellar halo in UFDs (Deason et al. 2022; Ricotti et al. 2022), show the impact of the progenitor size on the radius of the post-merger galaxy, and highlight the possibility of inferring progenitor and merger properties using present-day observations. The agreement between the results from our simulations and emulations with observations in terms of  $f_5$ ,  $R_*$ , and stellar surface density further corroborates the merging scenario suggested by observations (Chiti et al. 2021, 2023) and simulations of two specific UFD progenitors (Tarumi et al. 2021).

We expect ongoing and future spectroscopic surveys targeting UFDs to have a high impact on the search for stellar halos. For example, 4DWARFS (Skúladóttir et al. 2023) will provide the chemical abundances for more than 2000 stars in  $\sim 40$  UFDs (Skúladóttir, private communication). The higher statistic will produce precise measurements of  $f_5$  in Tucana II and possibly other UFDs, revealing the frequency of stellar halos around UFDs. Using our method on this upcoming data will allow us to uncover the past assembly history of the faintest companions of our Milky Way.

*Acknowledgements.* This project received funding from the ERC Starting Grant NEFERTITI H2020/804240 (PI: Salvadori). We acknowledge the CINECA award under the ISCRA initiative, for the availability of high performance computing resources and support from the Class C project UFD-SHF, “UFD mergers: Stellar Halo Formation”, HP10CM106H (PI: Querci). We acknowledge the usage of AREPO (Weinberger et al. 2020), ASTROPY (Collaboration et al. 2022), DEEPXDE (Lu et al. 2021), DICE (Perret 2016), MATPLOTLIB (Hunter 2007), NUMPY (Harris et al. 2020), PYNBODY (Pontzen et al. 2013), PYTHON3 (Van Rossum & Drake 2009), SCIPY (Virtanen et al. 2020), and SCIKIT LEARN (Pedregosa et al. 2011).

## References

- Agertz, O., Pontzen, A., Read, J. I., et al. 2020, *MNRAS*, 491, 1656  
 Bagla, J. S. 2002, *Journal of Astrophysics and Astronomy*, 23, 185  
 Barkana, R. & Loeb, A. 1999, *ApJ*, 523, 54  
 Barnes, J. & Hut, P. 1986, *Nature*, 324, 446  
 Bartlett, D. J., Chiarenza, M., Doerer, L., & Leclercq, F. 2024, COmoving Computer Acceleration (COCA):  $N$ -body simulations in an emulated frame of reference  
 Battaglia, G. & Nipoti, C. 2022, *Nature Astronomy*, 6, 659  
 Bechtol, K., Drlica-Wagner, A., Balbinot, E., et al. 2015, *ApJ*, 807, 50  
 Behroozi, P. S., Wechsler, R. H., & Conroy, C. 2013, *ApJ*, 770, 57  
 Belokurov, V., Zucker, D. B., Evans, N. W., et al. 2006, *ApJL*, 647, L111  
 Bird, S., Rogers, K. K., Peiris, H. V., et al. 2019, *JCAP*, 2019, 050  
 Branca, L. & Pallottini, A. 2024, *A&A*, 684, A203  
 Brown, S. T., Fattahi, A., McCarthy, I. G., et al. 2024, *MNRAS*, 532, 1223  
 Brown, T. M., Tumlinson, J., Geha, M., et al. 2012, *ApJL*, 753, L21  
 Bühlmann, P. & van de Geer, S. 2011, *Statistics for High-Dimensional Data: Methods, Theory and Applications*, Springer Series in Statistics (Springer Berlin, Heidelberg)

- Bullock, J. S. & Boylan-Kolchin, M. 2017, *ARA&A*, 55, 343
- Chiti, A., Frebel, A., Ji, A. P., et al. 2018, *ApJ*, 857, 74
- Chiti, A., Frebel, A., Ji, A. P., et al. 2023, *AJ*, 165, 55
- Chiti, A., Frebel, A., Simon, J. D., et al. 2021, *Nature Astronomy*, 5, 392
- Collaboration, T. A., Price-Whelan, A. M., Lim, P. L., et al. 2022, *The Astrophysical Journal*, 935, 167
- Cybenko, G. 1989, *Mathematics of Control, Signals, and Systems (MCSS)*, 2, 303
- Deason, A., Wetzel, A., & Garrison-Kimmel, S. 2014, *ApJ*, 794, 115
- Deason, A. J., Bose, S., Fattahi, A., et al. 2022, *MNRAS*, 511, 4044
- Di Cintio, P. 2024, *A&A*, 683, A254
- Diemer, B. & Kravtsov, A. V. 2015, *ApJ*, 799, 108
- Errani, R., Peñarrubia, J., & Walker, M. G. 2018, *MNRAS*, 481, 5073
- Fattahi, A., Navarro, J. F., Frenk, C. S., et al. 2018, *MNRAS*, 476, 3816
- Gallart, C., Monelli, M., Ruiz-Lara, T., et al. 2021, *ApJ*, 909, 192
- Garling, C., Willman, B., Sand, D. J., et al. 2018, *ApJ*, 852, 44
- Gelli, V., Salvadori, S., Ferrara, A., Pallottini, A., & Carniani, S. 2023, *ApJL*, 954, L11
- Gelli, V., Salvadori, S., Pallottini, A., & Ferrara, A. 2020, *MNRAS*, 498, 4134
- Goater, A., Read, J. I., Noël, N. E. D., et al. 2024, *MNRAS*, 527, 2403
- Gutcke, T. A., Pfrommer, C., Bryan, G. L., et al. 2022, *ApJ*, 941, 120
- Hansen, T. T., Simon, J. D., Li, T. S., et al. 2024, *ApJ*, 968, 21
- Harris, C. R., Millman, K. J., van der Walt, S. J., et al. 2020, *Nature*, 585, 357
- Hunter, J. D. 2007, *Computing in Science & Engineering*, 9, 90
- Jensen, J., Hayes, C. R., Sestito, F., et al. 2024, *MNRAS*, 527, 4209
- Jeon, M., Besla, G., & Bromm, V. 2017, *ApJ*, 848, 85
- Jeon, M., Bromm, V., Pawlik, A. H., & Milosavljević, M. 2015, *MNRAS*, 452, 1152
- Ji, A. P., Frebel, A., Ezzeddine, R., & Casey, A. R. 2016, *ApJL*, 832, L3
- Kirby, E. N., Simon, J. D., Geha, M., Guhathakurta, P., & Frebel, A. 2008, *ApJL*, 685, L43
- Lai, D. K., Lee, Y. S., Bolte, M., et al. 2011, *ApJ*, 738, 51
- Li, T. S., Simon, J. D., Kuehn, K., et al. 2018, *ApJ*, 866, 22
- Longeard, N., Jablonka, P., Battaglia, G., et al. 2023, *MNRAS*, 525, 3086
- Lu, L., Meng, X., Mao, Z., & Karniadakis, G. E. 2021, *SIAM Review*, 63, 208
- Ludlow, A. D., Fall, S. M., Wilkinson, M. J., Schaye, J., & Obreschkow, D. 2023, *MNRAS*, 525, 5614
- Magg, M., Hartwig, T., Agarwal, B., et al. 2018, *MNRAS*, 473, 5308
- Martin, N. F., de Jong, J. T. A., & Rix, H.-W. 2008, *ApJ*, 684, 1075
- McConnachie, A. W. 2012, *AJ*, 144, 4
- McKay, M. D., Beckman, R. J., & Conover, W. J. 1979, *Technometrics*, 21, 239
- Muñoz, R. R., Côté, P., Santana, F. A., et al. 2018, *ApJ*, 860, 66
- Navarro, J. F., Frenk, C. S., & White, S. D. M. 1996, *ApJ*, 462, 563
- Oogi, T., Habe, A., & Ishiyama, T. 2015, *Monthly Notices of the Royal Astronomical Society*, 456, 300
- Ou, X., Chiti, A., Shipp, N., et al. 2024, *ApJ*, 966, 33
- Pace, A. B., Erkal, D., & Li, T. S. 2022, *ApJ*, 940, 136
- Pallottini, A. & Ferrara, A. 2023, *A&A*, 677, L4
- Peñarrubia, J., Navarro, J. F., & McConnachie, A. W. 2008, *ApJ*, 673, 226
- Pedregosa, F., Varoquaux, G., Gramfort, A., et al. 2011, *Journal of Machine Learning Research*, 12, 2825
- Perret, V. 2016, ASCL.net - DICE: Disk Initial Conditions Environment, Astrophysics Source Code Library, record ascl:1305.002
- Planck Collaboration. 2016, *A&A*, 594, A13
- Poggio, T. & Liao, Q. 2018, *Bulletin of the Polish Academy of Sciences: Technical Sciences*, 66, 761
- Pontzen, A., Roškar, R., Stinson, G., & Woods, R. 2013, pynbody: N-Body/SPH analysis for python, Astrophysics Source Code Library, record ascl:1305.002
- Revaz, Y. 2023, *A&A*, 679, A2
- Ricotti, M. & Gnedin, N. Y. 2005, *ApJ*, 629, 259
- Ricotti, M., Polisensky, E., & Cleland, E. 2022, *MNRAS*, 515, 302
- Robinson, D., Avestruz, C., & Gnedin, N. Y. 2024, *arXiv e-prints*, arXiv:2406.19446
- Rogers, K. K., Peiris, H. V., Pontzen, A., et al. 2019, *JCAP*, 2019, 031
- Rossi, M., Salvadori, S., Skúladóttir, Á., & Vanni, I. 2023, *MNRAS*, 522, L1
- Rossi, M., Salvadori, S., Skúladóttir, Á., Vanni, I., & Koutsouridou, I. 2024, *arXiv e-prints*, arXiv:2406.12960
- Salvadori, S. & Ferrara, A. 2009, *MNRAS*, 395, L6
- Salvadori, S., Skúladóttir, Á., & Tolstoy, E. 2015, *MNRAS*, 454, 1320
- Simon, J. D. 2019, *ARA&A*, 57, 375
- Skúladóttir, Á., Puls, A. A., Amarsi, A. M., et al. 2023, *The Messenger*, 190, 19
- Sobacchi, E. & Mesinger, A. 2013, *MNRAS*, 432, 3340
- Spite, M., Spite, F., François, P., et al. 2018, *A&A*, 617, A56
- Springel, V. 2010, *MNRAS*, 401, 791
- Springel, V., Yoshida, N., & White, S. D. M. 2001, *New Astronomy*, 6, 79
- Spurio Mancini, A., Piras, D., Alsing, J., Joachimi, B., & Hobson, M. P. 2022, *MNRAS*, 511, 1771
- Strigari, L. E. 2018, *Reports on Progress in Physics*, 81, 056901
- Sun, G., Faucher-Giguère, C.-A., Hayward, C. C., & Shen, X. 2023, *MNRAS*, 526, 2665
- Tarumi, Y., Yoshida, N., & Frebel, A. 2021, *ApJL*, 914, L10
- Tau, E. A., Vivas, A. K., & Martínez-Vázquez, C. E. 2024, *AJ*, 167, 57
- Van Rossum, G. & Drake, F. L. 2009, *Python 3 Reference Manual* (Scotts Valley, CA: CreateSpace)
- Virtanen, P., Gommers, R., Oliphant, T. E., et al. 2020, *Nature Methods*, 17, 261
- Waller, F., Venn, K. A., Sestito, F., et al. 2023, *MNRAS*, 519, 1349
- Weinberger, R., Springel, V., & Pakmor, R. 2020, *ApJS*, 248, 32
- Westmeier, T., Staveley-Smith, L., Calabretta, M., et al. 2015, *MNRAS*, 453, 338
- Wheeler, C., Hopkins, P. F., Pace, A. B., et al. 2019, *MNRAS*, 490, 4447
- Wolf, J., Martínez, G. D., Bullock, J. S., et al. 2010, *MNRAS*, 406, 1220
- Yoon, J., Beers, T. C., Tian, D., & Whitten, D. D. 2019, *ApJ*, 878, 97

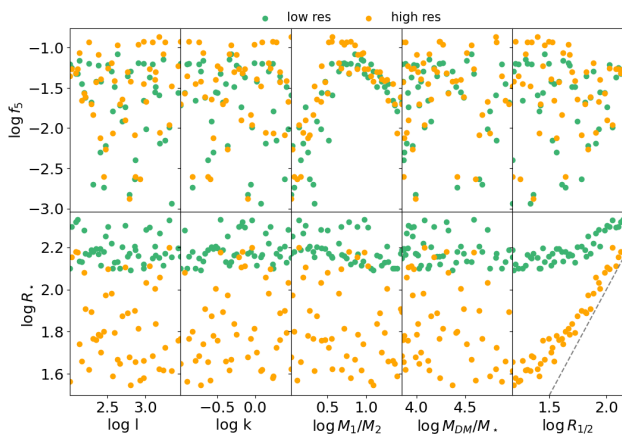


Fig. A.1: Comparison of the distribution of the post-merger galaxies properties, i.e., half-mass radius  $R_*$  (bottom row) and fraction of stars  $f_5$  beyond  $5R_*$  (top row), changing the dark matter resolution. Each column represents an initial condition property explored in this work, from left to right are: specific angular momentum  $l$ , specific kinetic energy  $k$ , merger mass ratio  $M_1/M_2$ , dark matter abundance  $M_{\text{DM}}/M_*$ , and progenitor half-mass radius  $R_{1/2}$ . The dashed line in the bottom right corner is  $R_* = R_{1/2}$ . The low resolution simulations ( $m_{\text{DM}}^{\text{low}} = 10^3 M_\odot$ ) are in green while in orange are the high resolution simulations ( $m_{\text{DM}}^{\text{high}} = 10^2 M_\odot$ ).

## Appendix A: Dynamical heating from dark matter resolution

Simulated galaxies can be susceptible to spurious evolution due to the finite number of particles with which they are resolved that can induce numerical heating, i.e., the massive dark matter particles heat the low-mass stars puffing up the galaxy. To test our results, we compare the post-merging galaxies of the low and high dark matter resolution suites,  $m_{\text{DM}}^{\text{low}} = 10^3 M_\odot$  and  $m_{\text{DM}}^{\text{high}} = 10^2 M_\odot$ , respectively. The suite resolution ratios are thus  $m_{\text{DM}}^{\text{low}}/m_* = 10^3$ , similar to Agertz et al. (2020), and  $m_{\text{DM}}^{\text{high}}/m_* = 10^2$ , consistent with Ricotti et al. (2022).

In Fig. A.1, we show the distribution of the post-merger galaxies properties,  $f_5$  top row and  $R_*$  bottom row, in the parameter space explored. The high-resolution simulations are in orange and the low-resolution in green. Comparing the distributions of the fraction of distant stars, we note that they overlap, with the higher resolution suite peaking at a higher value ( $\sim 13\%$ ) compared to the low-resolution ( $\sim 8.2\%$ ). On the contrary, the half-mass distributions do not overlap, with the low-resolution  $R_*$  systematically higher than the high-resolution one.

Considering the typical error estimating  $f_5$ , i.e., of the order of 20%, the  $f_5$  distributions at different resolutions are consistent. Such consistency confirms that the simulations capture the stellar halo formation by a *dry* merger, even with a resolution as low as  $m_{\text{DM}}^{\text{low}}$ . On the contrary, the half-mass radius distributions do not overlap, even considering the error associated with the measure, showing the impact of spurious numerical heating and forcing a different method to test the convergence of the simulations. The size of the post-merger galaxy (orange points) is larger than the progenitor radius (the dashed line), as expected in N-body *dry* mergers simulations (Oogi et al. 2015) and evident from the bottom right panel of Fig. A.1. For  $R_{1/2} > 50$  pc, the two radii are proportional, while below 50 pc  $R_*$  saturates

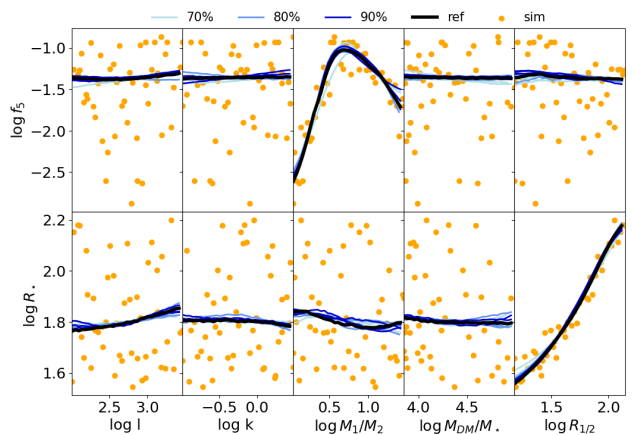


Fig. B.1: Same as Fig. A.1 considering only the high resolution simulation data in orange. Each line represents the median distribution of the reference emulator, black, or the test emulator, colored in shades of blue based on the size of the training set.

at a minimum value, i.e., the radius resolution limit, suggesting that the numerical heating can be neglected in simulations with  $R_{1/2} > 50$  pc. To further verify that numerical heating is negligible, we limit  $R_{1/2}$  to the proportional regime and determine the impact of each parameter on  $R_*$ . We find the same hierarchy as when using the whole dataset, with  $R_{1/2}$  being the dominant parameter and  $M_1/M_2$  playing a secondary role, showing that numerical heating does not affect our results. Moreover, the values of  $R_*$  derived at  $R_{1/2} \simeq 100$  pc, i.e., the expected value of the massive progenitor radius consistent with observations, for different resolutions are consistent when considering the observational errors are of the order of  $\sim 30$  pc.

For the reasons stated above, our results on the stellar halo formation and size of the post-merger galaxies are well captured by the dark matter resolution  $m_{\text{DM}}^{\text{high}} = 10^2 M_\odot$ , and there is no need for increasing the resolution.

## Appendix B: Using Neural Networks as an emulator

In this work, we adopt and train a neural network as an emulator to infer an approximate value of  $f_5$  and  $R_*$  of post-merger galaxies based on the initial conditions of the merger. The NN has an input layer with 5 neurons, one for each parameter explored, i.e.,  $l$ ,  $k$ ,  $M_1/M_2$ ,  $M_{\text{DM}}/M_*$ , and  $R_{1/2}$ , 5 hidden layers with 128 dense neurons, and an output layer with a neuron for  $f_5$  and  $R_*$ , each.

The number of simulations available for training and testing the NN is limited, and each simulation carries information in a specific interval of initial conditions. To avoid losing information, we train the NN on all the available data, and we use a l2 regularization to control overfitting (Bühlmann & van de Geer 2011). We tested our approach by training nine identical emulators on 90%, 80%, and 70% of the dataset and testing them on the remaining fraction.

Fig. B.1 shows the median of the inferred values of all emulators, colored by the training data size. All medians do not deviate more than 0.1 dex between each other, 0.05 dex in some cases, confirming that using all the available data to train the NN does not affect the results. Moreover, the primary and secondary dependencies on the initial conditions properties and the inferred value of  $M_1/M_2$  and  $R_{1/2}$  are consistent between all emulators, corroborating that our results do not critically depend on the training set of the NN.